Domain decomposition non-intrusive reduced order modelling of non-linear flow dynamics

D. Xiao[a,*], F. Fang[a], C.C. Pain[a], I.M. Navon[b]

[a]*Applied Modelling and Computation Group, Department of Earth Science and Engineering, Imperial College London, Prince Consort Road, London, SW7 2BP, UK.URL:* `http://amcg.ese.imperial.ac.uk`
[b]*Department of Scientific Computing, Florida State University,Tallahassee, FL, 32306-4120, USA*

Abstract

In this paper we first introduce the domain decomposition (DD) technique into non-intrusive reduced order modelling for complex non-linear fluid dynamics problems. The computational domain is partitioned into subdomains representing different physical and flow features, such as shock waves, moving fronts and eddies. A set of local basis functions for each subdomain is constructed using the proper orthogonal decomposition (POD) method. The radial basis function (RBF) methods are then used to generate a set of local hypersurfaces for each subdomain. These local hypersurfaces can represent not only the fluid dynamics over the subdomain it belongs to, but also the interaction between this subdomain and the surrounding subdomains.

Specifically, we have developed a domain decomposition non-intrusive reduced order model (DDNIROM) for the Navier-Stokes equations. The performance of this DDNIROM is numerically illustrated by two examples, flow past a cylinder and street canyon, respectively. The results show that the DDNIROM exhibits good agreement with the high fidelity full model while the computational cost is reduced by several orders of magnitude. By using the DD method, the DDNIROM can provide the details of local non-linear flow features isolated within each subdomain, for example, eddies around the cylinder and within the street canyons. It also provides the flexibility to choose different numbers of local basis functions for each subdomain, thus reducing the need for large multidimensional hypersurfaces representing the fluid dynamics using the global NIROM.

Keywords: domain decomposition, reduced order modelling, non-intrusive, proper orthogonal decomposition

1. Introduction

Reduced order modelling (ROM) is a powerful tool for real-time analysis as it offers the potential to reduce dimensionality of large complex systems. ROM has been

*Corresponding author
Email address: `dh.xiao@imperial.ac.uk` (D. Xiao)

successfully applied to various fields, for example, fracture modelling [1], fluid dynamics [2, 3, 4, 5, 6, 7], air pollution [8], molecular dynamics [9], aerospace design [10], parameter optimization [11] and haemodynamics [12]. Proper orthogonal decomposition (POD) in combination with Galerkin projection is the most popular method used for deriving a reduced order model. However, this method is dependent on the original source code and has some disadvantages such as instability and non-linear inefficiency [13, 14, 15, 16, 17]. To tackle those issues, a number of stabilisation methods have been presented, for example, Petrov-Galerkin method [18, 19], calibration [20, 21], regularisation [22] and Fourier expansion [23]. Also, various non-linearity model reduction methods have been proposed such as empirical interpolation method (EIM) [24], discrete EIM (DEIM) [16], residual DEIM (RDEIM) [25], Petrov−Galerkin projection [20], Gauss−Newton with approximated tensors (GNAT) [26] and the quadratic expansion method [27].

More recently, the non-intrusive reduced order modelling (NIROM) is becoming popular in various research and engineering fields as its implementation is independent of the original source code. The applications include fluid problems [28, 29, 30, 31, 32], fluid-structure interaction problems [33, 34] and multiphase porous media flows [35, 36]. Xiao *et al.* [37] also presented a parameterized NIROM for general time-dependent nonlinear partial differential equations. However, POD ROM has its difficulty in capturing every location traversed by a moving discontinuity, which requires larger number of basis functions and larger amount of data in order to capture the energy [38]. This motivates the development of subdomain ROM technology for complex flows (*e.g.* turbulent flows) and localized complex physical problems, *e.g.* traffic, chemistry, greening, particles and radiation. Using DD approach allows us to construct different local basis functions based on details of local flow solutions over each subdomains.

The domain decomposition method originated in the work of Przemieniecki [39]. It has been applied to various fields, such as parallel processing [40, 41], shear bands [42], stochastic multiphysics systems [43] and hydrodynamics [44]. Lucia *et al.* [38] first introduced the DD method to reduced order modelling for accurately tracking a moving strong shock wave. Baiges *et al.* [45], Amsallem *et al.* [46] and Chaturantabut [47] applied the DD method to non-linear model reduction. Kerfriden *et al.* [48] proposed a partitioned ROM strategy for nonlinear fracture problems. Pau *et al.* [49, 50] used the POD mapping method to construct ROMs for fine-resolution river basin models.

This paper presents a new subdomain non-intrusive reduced order model for fluid problems using the POD and radial basis function (RBF) methods. The key idea underpinning this DDNIROM is to introduce the DD method to our recently developed non-intrusive reduced order modelling technique based on the RBF. It is a robust and efficient approach for model reduction of general linear and non-linear time-dependent flow dynamical systems, even when source code is unavailable. Using the RBF method, a set of local hypersurfaces for each subdomain is constructed in such a way as to represent the underlying reduced flow dynamics from both this subdomain and its neighboring subdomains.

In DDNIROM, during the offline computational procedure, the solutions to the high fidelity model are recorded as a sequence of snapshots over the computational domain and thus partitioned into subdomains according to local flow features. From

the local solution snapshots over each subdomain, a number of local basis functions are generated using POD. The RBF multi-dimensional interpolation method is then used to construct a set of local hypersurfaces representing the local fluid dynamics over this subdomain. When constructing the local hypersurfaces for the subdomain, the energy of the surrounding subdomains associated to this subdomain is taken into account.

During the online computational procedure, for each subdomain, the solution of the DDNIROM at the current time level can be obtained by providing the reduced solutions at the previous time level over the current subdomain, as well as that at the current time level over its surrounding subdomains into the local hypersurface functions. The performance of the new DDNIROM has been assessed through two fluids test cases: flow past a cylinder and street canyon test cases. Comparisons between the high fidelity full model and the proposed DDNIROM have been carried out to validate the accuracy of the new DDNIROM.

The structure of the present paper is as follows. Section 2 presents the governing equations of fluid problems. Section 3 describes the general theory of the non-intrusive reduced order model (NIROM). Section 4 derives the methods of constructing a subdomain non-intrusive reduced order model (DDNIROM) for fluids problems. Section 5 demonstrates the performance of the DDNIROM for two numerical cases: flow past a cylinder and street canyon test cases. Finally in section 6, summary and conclusions are presented.

2. Governing equations for fluid dynamics

This work uses the non-hydrostatic Navier-Stokes equations to describe the fluid dynamics, namely,

$$\nabla \cdot \mathbf{u} = 0, \tag{1}$$

$$\frac{\partial \mathbf{u}}{\partial t} + \mathbf{u} \cdot \nabla \mathbf{u} + f\mathbf{k} \times \mathbf{u} = -\nabla p + \nabla \cdot \tau, \tag{2}$$

where $\mathbf{u} \equiv (u, v, w)^T$ is the velocity vector, p is the perturbation pressure ($p := p/\rho_0$, ρ_0 is the constant reference density), f represents the Coriolis inertial force, and $\mathbf{k}$ is an unit vector along the vertical direction. The stress tensor τ in the diffusion term is used to represent the viscous terms and is defined in terms of the deformation rate tensor $\mathbf{S}$ as

$$\tau_{ij} = 2\mu_{ij}S_{ij}, \quad S_{ij} = \frac{1}{2}\left(\frac{\partial u_i}{\partial x_j} + \frac{\partial u_j}{\partial x_i}\right) - \frac{1}{3}\sum_{k=1}^{3}\frac{\partial u_k}{\partial x_k}, \quad 1 \le i, j \le 3, \tag{3}$$

where, μ is the kinematic viscosity. In the previous definition, we assume no summation over repeated indices. In this paper, the horizontal kinematic viscosities (μ_{11}, μ_{22}) and vertical kinematic viscosity (μ_{33}) assume constant values with the off-diagonal components of τ defined by $\mu_{ij} = (\mu_{ii}\mu_{jj})^{1/2}$.

3. Non-intrusive model reduction method

The essence of the non-intrusive model reduction methods consists in constructing a set of hypersurfaces that represent the reduced system. In POD methods, any variable

Ψ (for example, velocity and pressure) can be expressed:

$$\Psi = \overline{\Psi} + \sum_{i=1}^{m} \alpha_i \Phi_i, \tag{4}$$

where, $\overline{\Psi}$ is the mean of the variables over the simulation period, m is the number of POD basis functions, α represents the POD coefficients needed to be calculated over the reduced space (solutions of the ROM) and Φ represents the POD basis functions. The POD basis functions can be obtained by performing the Singular Value Decomposition (SVD) procedure.

The POD coefficients α can be derived by a multi-dimensional radial basis function interpolation method. In RBF multi- dimensional interpolation, a function $f(x)$ can be approximated by the linear combination of a number of RBFs ϕ centered at N points. There are various types of RBFs such as: multi-quadric, plate spline, Gaussian and inverse multi-quadric. In this paper we use the Gaussian RBF, which has a form of $\phi(r) = e^{-(r/\sigma)^2}$ (σ being the shape parameter and r being the radius). In NIROM, the POD coefficients α_i^t associated to the i^{th} POD basis function at any time level t can be obtained [29]:

$$\alpha_i^t = f_i(\alpha_1^{t-1}, \alpha_2^{t-1}, \cdots, \alpha_m^{t-1}), \tag{5}$$

The hypersurface f_i can be approximated by a linear combination of a number of RBFs [29]:

$$f_i(\alpha_1^{t-1}, \alpha_2^{t-1}, \cdots, \alpha_m^{t-1}) = \sum_{j=1}^{N} w_{i,j} \phi_j(\left\|(\alpha_1^{t-1}, \alpha_2^{t-1}, \cdots, \alpha_m^{t-1}) - \mathbf{C}\right\|), \tag{6}$$

where, N is the number of data points, the center $\mathbf{C}$ is chosen to be the origin of the input data. After obtaining the hypersurface f_j, the solutions at current time level can be obtained by inputting the solutions at previous time level [29].

4. Domain decomposition non-intrusive model reduction strategy

This section describes the strategy of deriving a general DDNIROM. In the newly proposed DDNIROM, the computational domain Ω is divided into S subdomains $\Omega^d, d \in \{1, 2, \cdots, S\}$ and each subdomain has local unknowns $\Psi^d \in \mathbb{R}^{L^d}, L = L_1 + \cdots + L^d + \cdots + L_S$. In this method, the variable solutions at nodes within the subdomain Ω^d are used for forming a set of local POD basis functions $\mathbf{\Phi}^d$. The local basis functions can be extended into global basis functions by assigning zero to other subdomains,

$$\mathbf{\Phi}_i = \begin{bmatrix} 0 \\ \vdots \\ \mathbf{\Phi}_i^d \\ \vdots \\ 0 \end{bmatrix}, \quad d \in \mathbb{R}^S, \quad i \in \mathbb{R}^m, \tag{7}$$

thereby ensuring orthonormality of the basis functions. The variables of solutions in the global domain then can be expressed by:

$$\Psi = \sum_{d=1}^{S} \mathbf{\Psi}^d, \tag{8}$$

$$\Psi^d = \overline{\Psi}^d + \sum_{i=1}^{m_d} \alpha_i^d \Phi_i^d, \tag{9}$$

where m_d is the numbers of basis functions for each subdomain Ω^d.

For each subdomain Ω^d, we construct a set of hypersurfaces f_i^d to represent the underlying dynamical system associated to this subdomain and the surrounding subdomains over the reduced space. Each hypersurface has the form of,

$$\alpha_i^{d,t} = f_i^d(\boldsymbol{\alpha}^{d,t-1}, \boldsymbol{\alpha}^{sd,t}), \tag{10}$$

where vector $\boldsymbol{\alpha}^{d,t-1}$ denotes the complete set of POD coefficients (for example, velocity $\boldsymbol{\alpha}_{\mathbf{u}}$, pressure $\boldsymbol{\alpha}_{\mathbf{p}}$) at previous time level $t-1$ for the subdomain Ω^d, $\boldsymbol{\alpha}^{sd,t}$ denotes the complete set of POD coefficients at time level t for the surrounding subdomains. In a 2-D case, the number of surrounding subdomains associated to this subdomain Ω^d is between 2 and 4, see a simple example in figure 1, which shows a maximum of four surrounding subdomains (labelled sd) connected with the subdomain Ω^d.

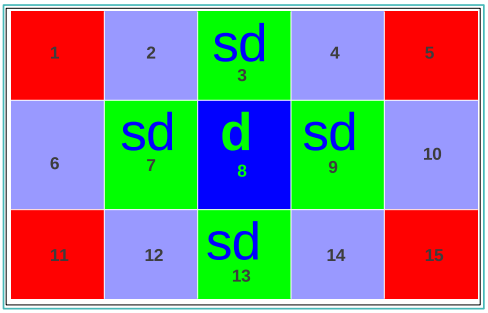

Figure 1: The figure shows a simple subdomain example, which uses colour to show the different subdomains clearly. The domain *d* has four surrounding subdomains-labelled *sd*.

The RBF/POD NIROM method is then used to construct a set of hypersurfaces for each POD coefficient at each subdomain. The procedure can be described in algorithms 1 (offline) and 2 (online), respectively. Algorithm 1 describes the offline computational procedure on how to construct a set of local hyper-surfaces for each subdomain while algorithm 2 details the online computation of DDNIROM where the interaction between a subdomain and its surrounding subdomains is taken into account.

Algorithm 1: Offline: constructing a set of hyper-surfaces for DDNIROM

(1) Generate a number of snapshots over the time period $[0, T]$ by solving the fluid dynamics problem;

(2) Divide the computational domain Ω into S subdomains;

(3) Generate a number of POD basis functions $\Phi_{\mathbf{u}}$ and Φ_p via performing SVD on the snapshots matrix of the subdomain;

(4) Obtain the functional values y^t at the data points $(\boldsymbol{\alpha}^{d,t-1}, \boldsymbol{\alpha}^{sd,t})$ via the solutions from the high fidelity model, where $t \in \{1, 2, \dots T\}$;

(5) Obtain a set of hypersurfaces through the following loop:

for $d = 1$ *to* S **do**
  for $i = 1$ *to* m **do**

(i) Calculate the weights $\mathbf{w}_{t,j}^d$ by solving equation (11);

$$A^d \mathbf{w}_{i,j}^d = y_{i,j}^d, \quad j \in \{1, 2, \dots, N\},$$

where A is a matrix associated with the radius, $A = \phi(r)$.

(ii) Obtain a set of hyper surfaces $(f_j^d(\alpha_1^{t-1}, \alpha_2^{t-1}, \cdots, \alpha_m^{t-1}))$ by substituting the weight values obtained in the above step into equation (11);

$$f_{\mathbf{u},i}^d(\alpha_{\mathbf{u}}^d, \alpha_p^d) = \sum_{j=1}^{N} w_{i,j}^d \phi_j^d(\left\|(\boldsymbol{\alpha}_{\mathbf{u}}^{d,t-1}, \boldsymbol{\alpha}_p^{d,t-1}, \boldsymbol{\alpha}_{\mathbf{u}}^{sd,t}, \boldsymbol{\alpha}_p^{sd,t}) - \mathbf{C}\right\|),$$

$$f_{p,i}^d(\alpha_{\mathbf{u}}^d, \alpha_p^d) = \sum_{i=1}^{N} w_{i,j}^d \phi_j^d(\left\|(\boldsymbol{\alpha}_{\mathbf{u}}^{d,t-1}, \boldsymbol{\alpha}_p^{d,t-1}, \boldsymbol{\alpha}_{\mathbf{u}}^{sd,t}, \boldsymbol{\alpha}_p^{sd,t}) - \mathbf{C}\right\|),$$

  endfor
endfor

Algorithm 2: Online DDNIROM calculation for the fluid problem

for $it = 1$ *to* $N_{iteration}$ **do**

for $d = 1$ *to* S **do**

(1) Obtain the surrounding subdomains (*sd* in figure 1) for the subdomain d according to the locations.

(2) Initialisation.

for $i = 1$ *to* m **do**

Initialize POD coefficients for subdomain d $(\boldsymbol{\alpha}^{d,0}_{\mathbf{u},j}, \boldsymbol{\alpha}^{d,0}_{p,j})$;

(3) Calculate solutions at current time step:

for $t = 1$ *to* T **do**

for $i = 1$ *to* m **do**

(i) Obtain the POD coefficients for associated surrounding subdomains. If there are no solutions for this surrounding subdomain, then ignore this surrounding subdomain at this iteration *it*.

(ii) Evaluate the hypersurfaces f^d at the previous time step $t-1$ by using the complete set of POD coefficients $\boldsymbol{\alpha}^{d,t-1}_{\mathbf{u},i}, \boldsymbol{\alpha}^{d,t-1}_{p,i}, \boldsymbol{\alpha}^{sd,t}_{\mathbf{u},i}, \boldsymbol{\alpha}^{sd,t}_{p,i}$:

$$f^d_{\mathbf{u},i} \leftarrow (\boldsymbol{\alpha}^{d,t-1}_{\mathbf{u},i}, \boldsymbol{\alpha}^{d,t-1}_{p,i}, \boldsymbol{\alpha}^{sd,t}_{\mathbf{u},i}, \boldsymbol{\alpha}^{sd,t}_{p,i}), \quad f^d_{p,i} \leftarrow (\boldsymbol{\alpha}^{d,t-1}_{\mathbf{u},i}, \boldsymbol{\alpha}^{d,t-1}_{p,i}, \boldsymbol{\alpha}^{sd,t}_{\mathbf{u},i}, \boldsymbol{\alpha}^{sd,t}_{p,i}), \tag{11}$$

(iii) Calculate the POD coefficients $\alpha^t_{\mathbf{u}}$ and α^t_p at the current time step t using the following equations:

$$\alpha^{d,t}_{\mathbf{u},i} = \sum_{t=1}^{T} w^d_{t,i}\phi^d_{t,j}(r), \quad \alpha^{d,t}_{p,i} = \sum_{t=1}^{T} w^d_{t,i}\phi^d_{t,i}(r), \tag{12}$$

for $d = 1$ *to* S **do**

Calculate the solutions $\mathbf{u}^{d,t}$ and $p^{d,t}$ for each subdomain d on the full space for each time step t by projecting $\alpha^{d,t}_{\mathbf{u},j}$ and $\alpha^{d,t}_{p,j}$ onto the full space.

$$\mathbf{u}^{d,t} = \bar{\mathbf{u}} + \sum_{j=1}^{m} \alpha^{d,t}_{\mathbf{u},j}\Phi^d_{\mathbf{u},j}, \quad p^{d,t} = \bar{p} + \sum_{j=1}^{m} \alpha^{d,t}_{p,j}\Phi^d_{p,j},$$

In algorithm 2, the iteration loop (**for** it = 1 to $N_{iteration}$) guarantees the hypersurface traverses the flow dynamics over/across the subdomain d and also all the surrounding subdomains *sd*. It ensures that the hypersurface represents the flow dynamics over the subdomain d, especially the flow interaction between the subdomain and the neighboring surrounding subdomains.

For example, when we solve the DDNIROM for each subdomain $\alpha^{d,t}_i$ at time level t, at the first iteration, we need the solutions over the subdomain, $\boldsymbol{\alpha}^{d,t-1}$ and $\boldsymbol{\alpha}^{sd,t-1}$

over the associated surrounding subdomains at the previous time level $t-1$. After the subdomain loop **for** d = 1 to **S** for the first iteration in algorithm 2, the solutions at current time level for each subdomain can be obtained. In the following iteration, the solutions $\boldsymbol{\alpha}^{sd,t}$ over surrounding subdomains at current time level t are updated. $\alpha_i^{d,t}$ can be obtained by inputting $\boldsymbol{\alpha}^{d,t-1}$ and $\boldsymbol{\alpha}^{sd,t}$ into the hypersurface.

5. Numerical examples

5.1. Case 1: flow past a cylinder

The DDNIROM is first validated in a dimensionless test case: flow past a cylinder, which is composed of a cylinder with a radius of 0.05 in the computational domain (2.2×0.41), see figure 2. The center of the cylinder is located at (0.25, 0.25). An inlet velocity of 1 is applied to the the left of the domain. The Reynolds number (*Re*) is set to be 3200. No normal flow and zero shear (slip) boundary conditions are applied to the cylinder and both lateral sides. There are 3213 nodes in the computational domain. In this example, the global domain is divided into 15 different subdomains, see figure 2. The simulational period is set to $[0, 6]$ with a time step size of $\Delta t = 0.01$. 60 snapshots (solutions obtained by running the high fidelity model) are taken at a regularly spaced time interval of 0.1.

Figure 3 shows the global and local singular eigenvalues (associated to the global and 15 subdomains respectively) in logarithmic scale in order of decreasing magnitude. The local basis function associated to a larger eigenvalue captures more energy in the original flow dynamic system over the subdomain. It can be seen in figure 3 that the local singular eigenvalues decrease faster than the global singular eigenvalues. Thus, in comparison to the global NIROM, a smaller number of local basis functions is required for capturing most of energy in the original flow dynamical system. This correspondingly reduces the dimension of hypersurfaces required for NIROM. To accurately represent the details of the flow around the cylinder, the subdomain 7 is further divided into 2×2 subdomains on average-labelled 16-19. Figure 4 shows the eigenvalues of the subdomain 7 and its sub-subdomains 16-19. Figures 5 and 6 show the first four leading basis functions associated to the global and subdomains 2, 7, 8 and 14. Again it can be seen that the local basis functions over these four subdomains capture more energy than the global basis functions.

Figure 3 provides us a criterion for choosing the number of local basis functions for each subdomain. The number of local basis functions for each subdomain (labeled in figure 2) is chosen in such a way that 99% of energy over the subdomain is captured by these selected local basis functions.

Figure 7 shows the velocity solutions obtained from the high fidelity full model and DDNIROM (the numbers of local basis functions for each subdomain are labeled in 2) at time level 5.0. As shown in the figure, the solutions from the DDNIROM are close to those from the high fidelity full model. The velocity solutions at a particular point ($x = 0.7184, y = 0.28652$) are shown in figure 8. As one can see from this figure, the DDNIROM with only 12 basis functions performs better than the global NIROM with 18 basis functions.

Figure 9 presents the root-mean-square error (RMSE) and the correlation coefficient of solutions between the high fidelity full model and both of the global NIROM

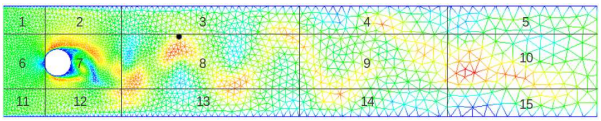

(a) subdomain number

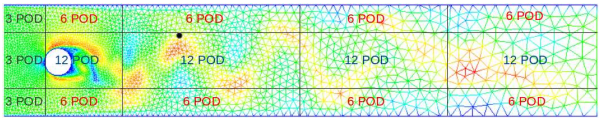

(b) distribution of number of POD

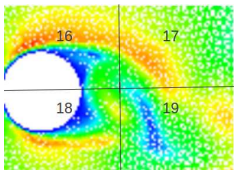

(c) subdomain 7

Figure 2: Case 1 - flow past a cylinder: the graphs shows the computational domain, number of basis functions distribution for each subdomain and 15 subdomains of the flow past a cylinder case.

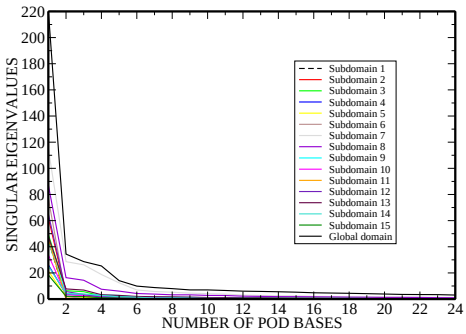

a(a) singular eigenvalues of all subdomains

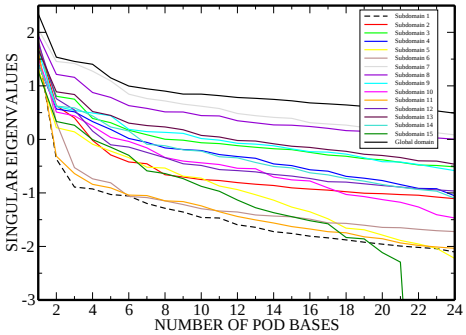

(b) logarithmic scale of singular eigenvalues

Figure 3: Case 1 - flow past a cylinder: the global and local singular eigenvalues associated to the global domain and 15 subdomains respectively.

and DDNIROM. We can see the correlation from the DDNIROM using 12 local basis functions is in closer agreement with the high fidelity full model than the global NIROM using 18 basis functions although there is no much difference in RMSE.

5.2. Case 2: urban street canyon test case

In the second example the DDNIROM is applied to the simulation of a 2D urban street canyon test case. The computational domain is shown in figure 10, consisting of a street canyon between two buildings. The domain has a dimensionless size of 2 $\times$ 1 and comprises of an unstructured finite element mesh with 8264 nodes, see figure 10. A uniform velocity of 1 is given to the left side of the computational domain as the inflow boundary condition. The top and bottom boundary conditions are free-slip and non-slip respectively. No-slip boundary conditions are prescribed to all the building surfaces. The kinematic viscosity is 1×10^{-4} and the Reynolds number based on the tallest building height is 1×10^4. The high fidelity full model was simulated for a time interval of $[0, 0.8]$ with a time step size of $\Delta t = 0.01$. Forty snapshots were taken at regularly spaced time levels of 0.02. In this example, the global domain was partitioned into 15 different subdomains, see figure 10.

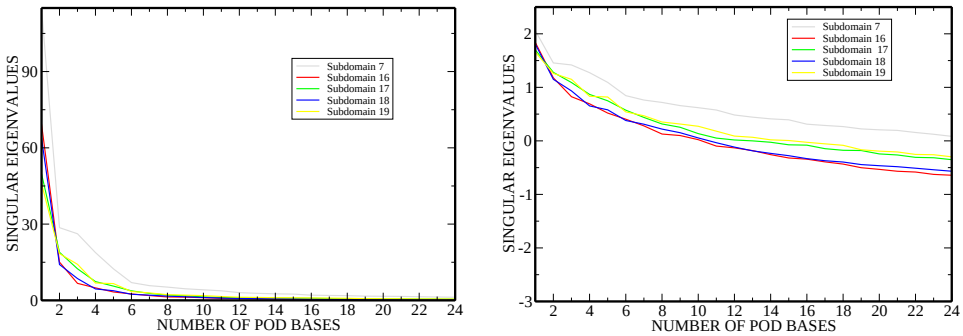

(a) singular eigenvalues (b) logarithmic scale of singular eigenvalues

Figure 4: Case 1 - flow past a cylinder: the singular eigenvalues over subdomain 7 and the subdomains inside the subdomain 7.

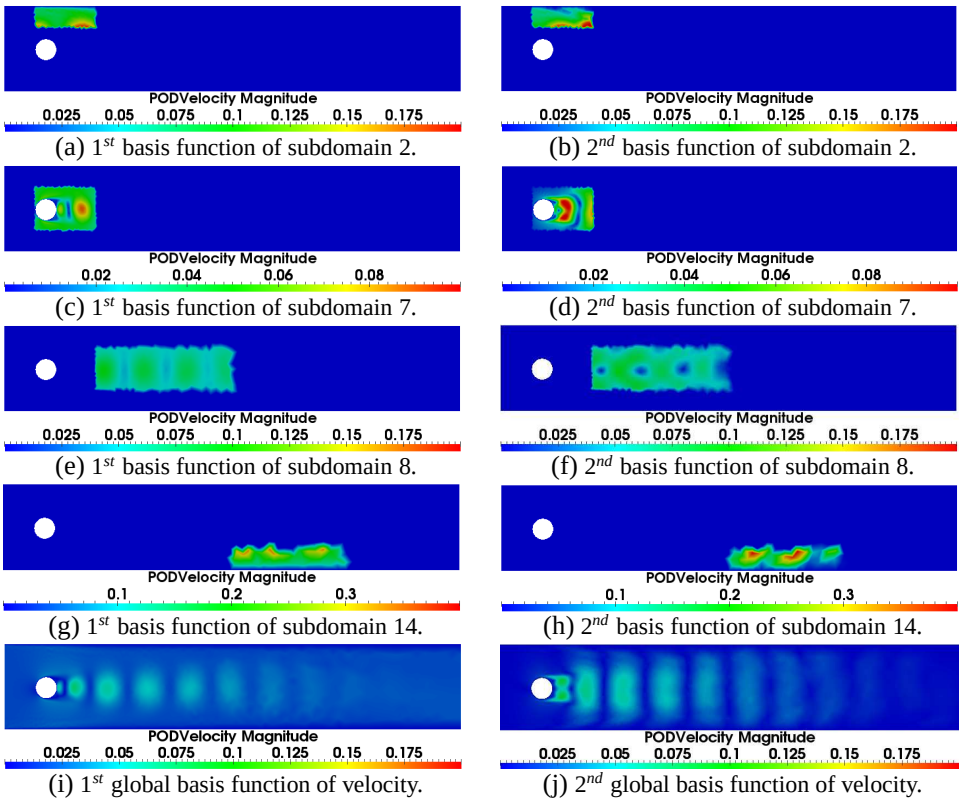

(a) 1^{st} basis function of subdomain 2.
(b) 2^{nd} basis function of subdomain 2.
(c) 1^{st} basis function of subdomain 7.
(d) 2^{nd} basis function of subdomain 7.
(e) 1^{st} basis function of subdomain 8.
(f) 2^{nd} basis function of subdomain 8.
(g) 1^{st} basis function of subdomain 14.
(h) 2^{nd} basis function of subdomain 14.
(i) 1^{st} global basis function of velocity.
(j) 2^{nd} global basis function of velocity.

Figure 5: Case 1 - flow past a cylinder: the first and second basis functions of the subdomain 2, 7, 8, 14 and global domain of velocity (including all components u and v) respectively.

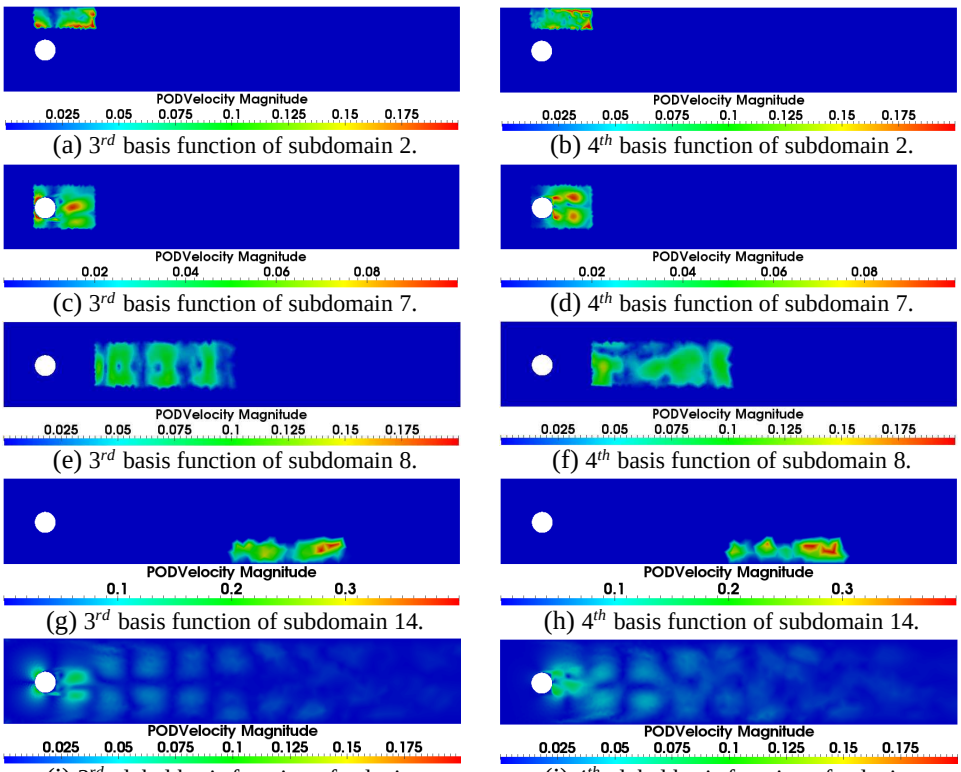

(a) 3^{rd} basis function of subdomain 2. (b) 4^{th} basis function of subdomain 2.

(c) 3^{rd} basis function of subdomain 7. (d) 4^{th} basis function of subdomain 7.

(e) 3^{rd} basis function of subdomain 8. (f) 4^{th} basis function of subdomain 8.

(g) 3^{rd} basis function of subdomain 14. (h) 4^{th} basis function of subdomain 14.

(i) 3^{rd} global basis function of velocity. (j) 4^{th} global basis function of velocity.

Figure 6: Case 1 - flow past a cylinder: the third and fourth basis functions of the velocity field over the global as well as the subdomain 2, 7, 8 and 14.

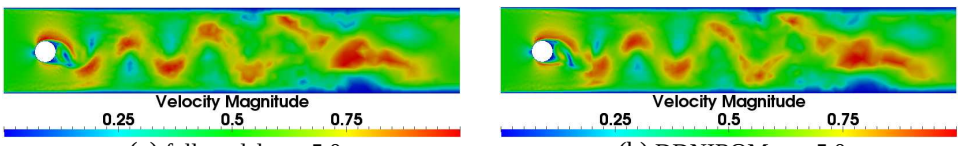

(a) full model, $t = 5.0$ (b) DDNIROM, $t = 5.0$

Figure 7: Case 1 - flow past a cylinder: the velocity solutions obtained from the full model and DDNIROM at time level 5.0. Note that the numbers of local basis functions for each subdomain are labelled in 2.

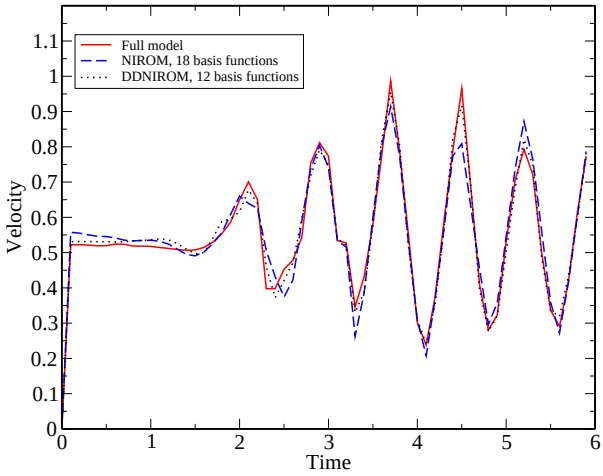

Figure 8: Case 1 - flow past a cylinder: the velocity solutions obtained from the high fidelity full model and global NIROM with 18 basis functions and DDNIROM (with 15 subdomains) with 12 basis functions at a particular point (x=0.7184, y=0.28652).

Figure 11 shows the global and local singular eigenvalues over the global domain and 15 subdomains respectively. Figure 12 shows the singular eigenvalues over subdomain 8 and the subdomains (16-21) inside the subdomain 8. Visually, the eigenvalues of subdomains (16-21) decay faster than those of subdomain 8 and the global domain. Different numbers of local basis functions are thus chosen for different subdomains in an optimal way that most of energy is captured. Figure 10 which shows the distribution of the number of basis functions for each subdomain. The graphs of the first four leading basis functions over the global domain and subdomains 2, 7, 8 and 12 are displayed in figures 13 and 14. These figures show that the local basis functions capture more energy and details than the global basis functions. It is seen that the flow structure within subdomain 8 is complex. To capture the details of eddies, subdomain 8 is further subdivided into 3×2 subdomains-labelled 16-21, see figure 10.

Figure 15 presents the velocity solutions at time level 0.6, as obtained from the full model and DDNIROM (using the numbers of local functions chosen for each subdomain shown in figure 10). It is minor visual differences of solutions between the two models. It can be seen from figure 15 that the DDNIROM captures well the small structures of the flow around the two buildings.

To further demonstrate the capability of the DDNIROM, only one and two local basis functions for all the subdomains are used to construct the DDNIROM. Figure 16 shows the velocity solutions at time level 0.4, calculated from the full model and both of the global NIROM and the DDNIROM. Figures 16 (f) and (g) show the error of velocity solutions from the NIROM and DDNIROM with 3 basis functions at time level 0.4. It can be seen that the DDNIROM captures well the eddies above the two buildings even using only 3 basis functions, and performs better than the global NIROM. This is further confirmed by the velocity solutions at a particular point ($x = 0.33221, y = 0.32814$) shown in figure 17. With increased number of basis

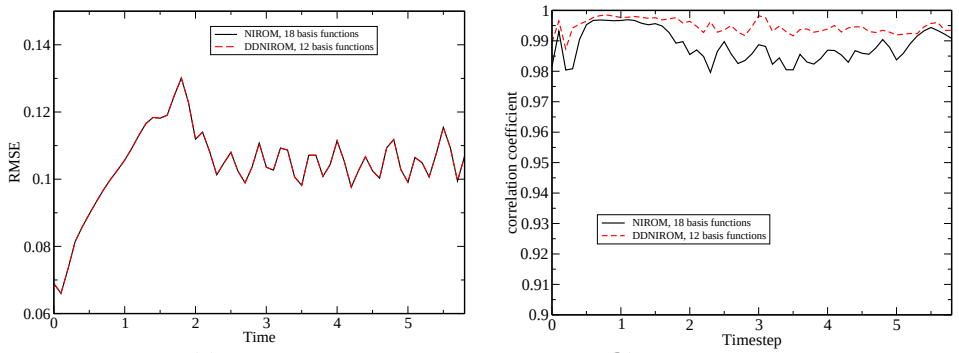

(a) RMSE (b) Correlation coefficient

Figure 9: Case 1: RMSE and correlation coefficient of velocity solutions between the high fidelity full model and both of the global NIROM with 18 basis function and the DDNIROM with 12 basis functions.

functions, the accuracy of solutions from the NIROMs has been improved. Again the DDNIROM with only 12 basis functions provides better results than the global NIROM with 18 basis functions, especially around the perturbation peak at $t = 0.04$. This is also highlighted by the correlation coefficient of velocity solutions, see figure 18. The reduction of basis functions required for NIROMs leads to a decreased dimension of hypersurfaces, thus decreasing the computational cost.

The computational cost of the DDNIROM is efficient. The CPU cost includes the offline and the online costs. The offline cost involves forming the basis functions and constructing the hypersurfaces. The CPU cost of forming the basis functions for the DDNIROM is almost equal to that of the global NIROM. The CPU cost of constructing the hypersurfaces can be ignored. The offline process is precomputed. The online CPU cost involves the time for solving the DDNIROM and projecting the reduced order results onto the full space. The online CPU cost required for DDNIROM only 0.016 second while 158 seconds for the fidelity full model. For large complex problems, the CPU time can be reduced by several orders of magnitude required for the fidelity full model.

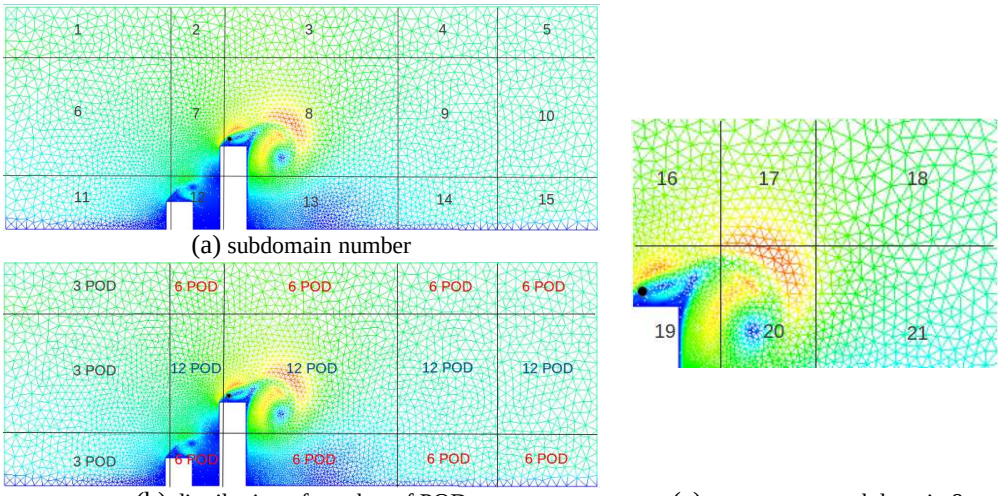

(a) subdomain number

(b) distribution of number of POD

(c) street canyon subdomain 8

Figure 10: Case 2 - urban street canyon test case: the 2D urban street canyon case: (a) the computational domain and 15 subdomains; (b) the number of POD basis functions chosen for each subdomain; and (c) 6 sub-subdomains within subdomain 8.

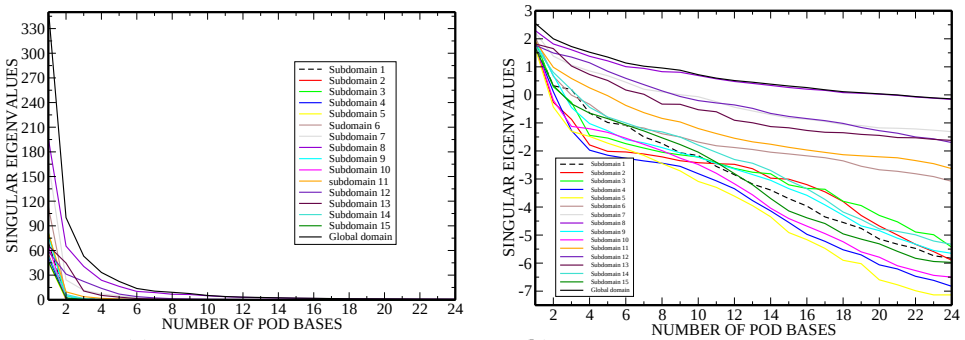

(a) singular eigenvalues

(b) logarithmic scale of singular eigenvalues

Figure 11: Case 2 - urban street canyon test case: the global and local singular eigenvalues over the global domain and 15 subdomains respectively.

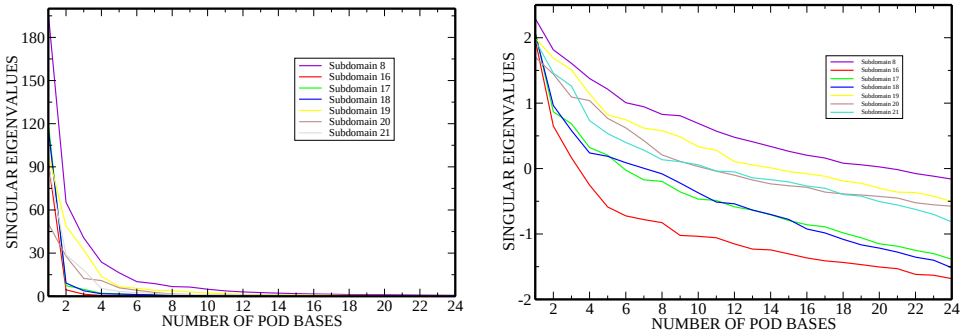

(a) singular eigenvalues of subdomain 8 (b) logarithmic scale of singular eigenvalues

Figure 12: Case 2 - urban street canyon test case: the singular eigenvalues associated to subdomain 8 and the subdomains inside the subdomain 8.

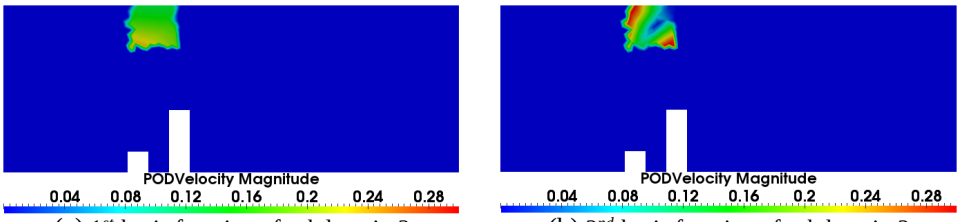

(a) 1^{st} basis function of subdomain 2.

(b) 2^{nd} basis function of subdomain 2.

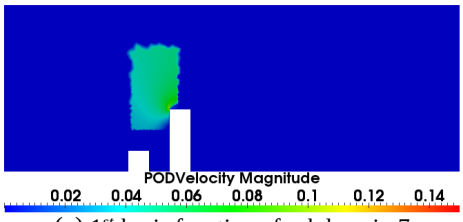

(c) 1^{st} basis function of subdomain 7.

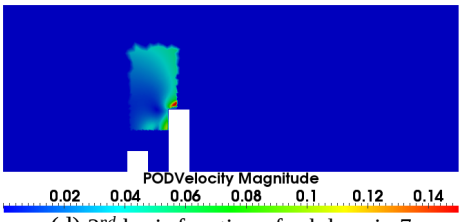

(d) 2^{nd} basis function of subdomain 7.

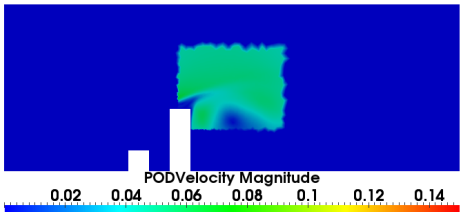

(e) 1^{st} basis function of subdomain 8.

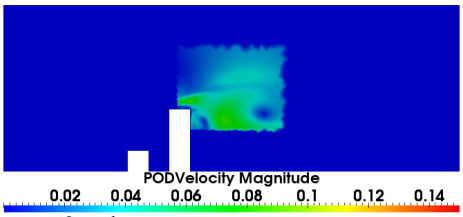

(f) 2^{nd} basis function of subdomain 8.

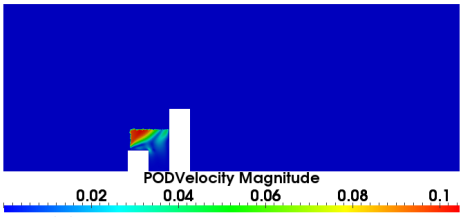

(g) 1^{st} basis function of subdomain 12.

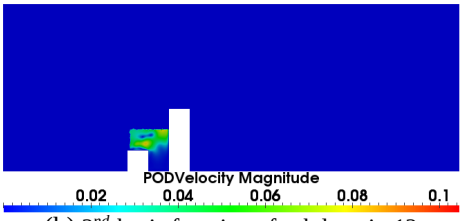

(h) 2^{nd} basis function of subdomain 12.

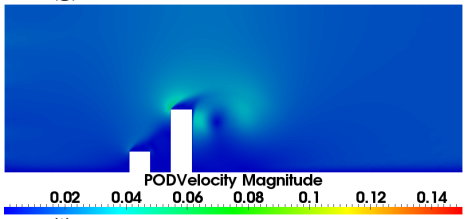

(i) 1^{st} global basis function of velocity.

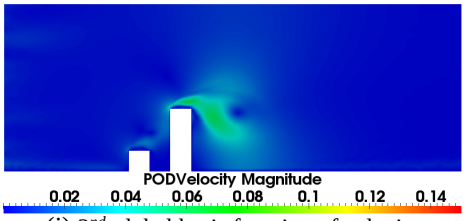

(j) 2^{nd} global basis function of velocity.

Figure 13: Case 2 - urban street canyon test case: the first and second basis functions and global functions of velocity (including all components u and v).

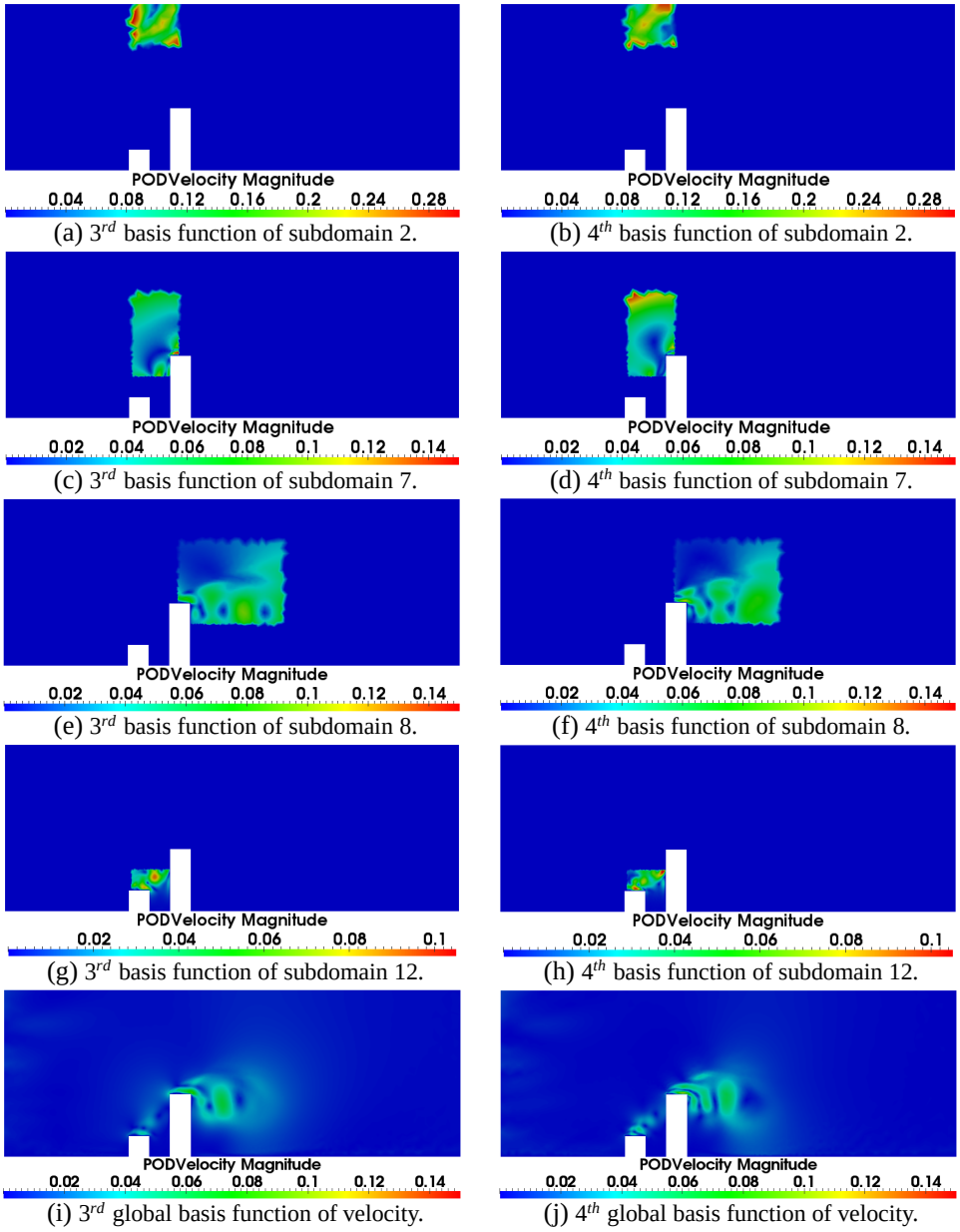

(a) 3^{rd} basis function of subdomain 2. (b) 4^{th} basis function of subdomain 2.

(c) 3^{rd} basis function of subdomain 7. (d) 4^{th} basis function of subdomain 7.

(e) 3^{rd} basis function of subdomain 8. (f) 4^{th} basis function of subdomain 8.

(g) 3^{rd} basis function of subdomain 12. (h) 4^{th} basis function of subdomain 12.

(i) 3^{rd} global basis function of velocity. (j) 4^{th} global basis function of velocity.

Figure 14: Case 2 - urban street canyon test case: the third and fourth basis functions and global basis functions of velocity (including all components u and v).

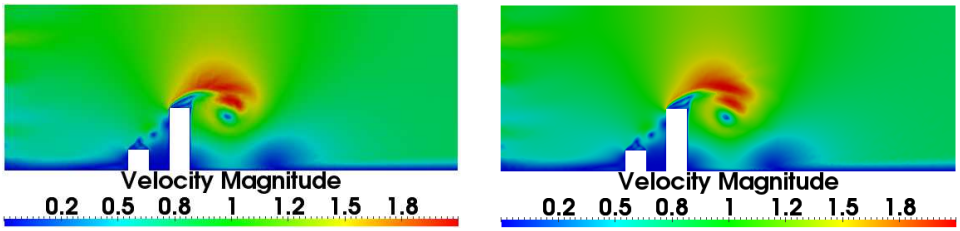

(a) full model, $t = 5.0$ (b) DDNIROM, $t = 5.0$

Figure 15: Case 2 - urban street canyon test case: the velocity solutions from the full model and DDNIROM at time level 5.The numbers of local functions chosen for each subdomain are shown in figure 10

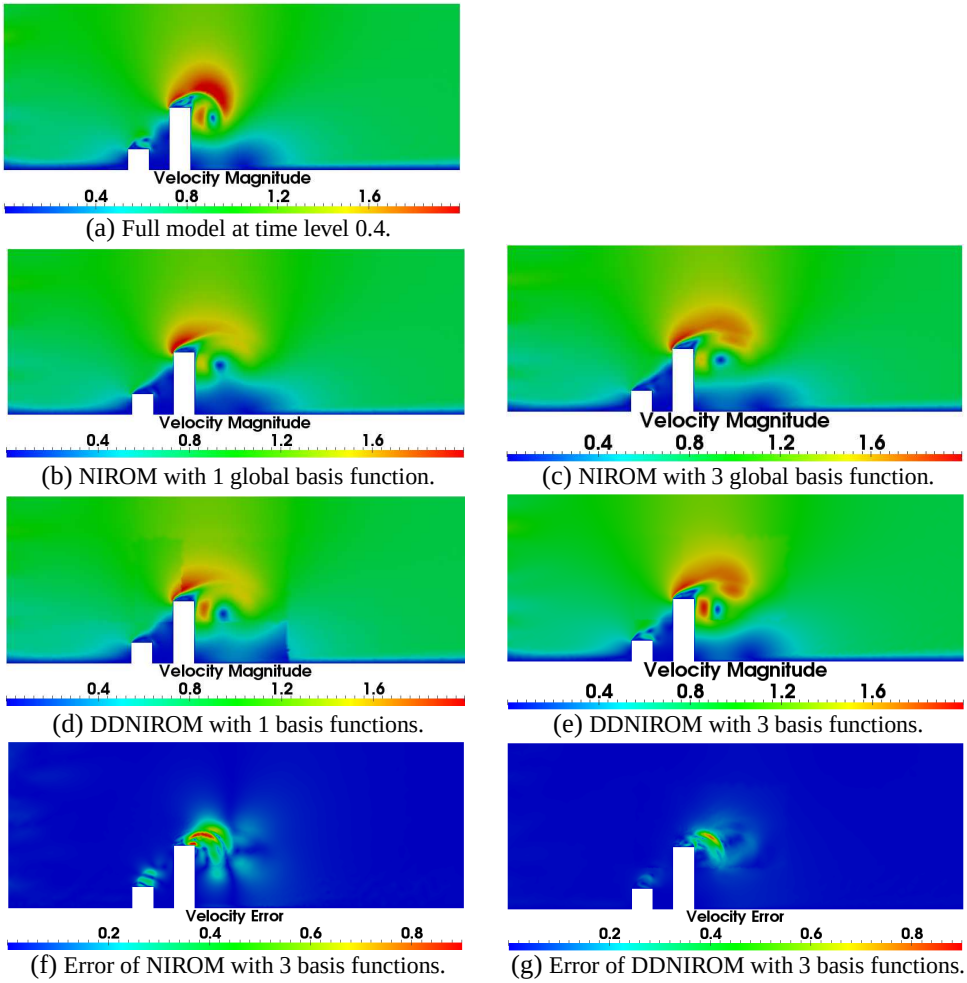

(a) Full model at time level 0.4.

(b) NIROM with 1 global basis function. (c) NIROM with 3 global basis function.

(d) DDNIROM with 1 basis functions. (e) DDNIROM with 3 basis functions.

(f) Error of NIROM with 3 basis functions. (g) Error of DDNIROM with 3 basis functions.

Figure 16: Case 2 - urban street canyon test case: figures (a) - (e) show the velocity solutions at time level 0.4, as calculated from the high fidelity full model and both of the global NIROM and DDNIROM with 1 basis function and 3 basis functions for all the subdomains; and figures (f) and (g) show the velocity errors from both the global NIROM and DDNIROM with 3 basis functions at time level 0.4.

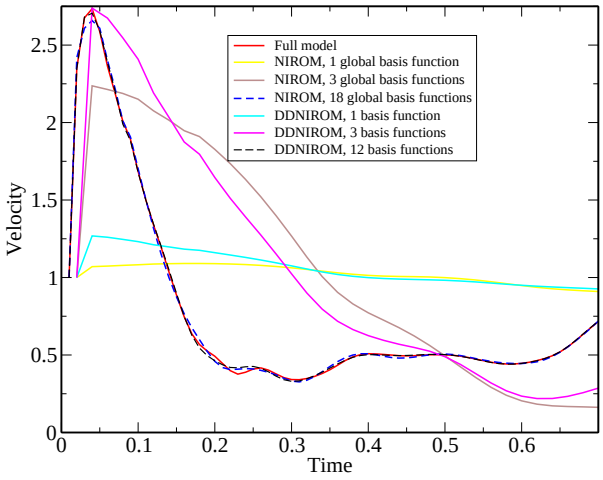

Figure 17: Case 2 - urban street canyon test case: the velocity solutions of the high fidelity full model, the global NIROM with 1, 3 and 18 global basis functions, as well as the DDNIROM with 1, 3 and 12 basis functions at a particular point (x=0.33221, y=0.32814).

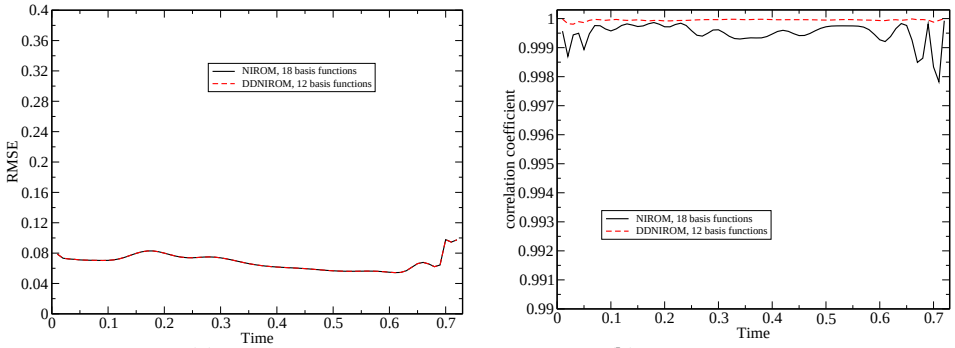

(a) RMSE (b) correlation coefficient

Figure 18: Case 2 - urban street canyon test case: RMSE and correlation coefficient of velocity solutions.

6. Conclusion

In this article, a domain decomposition non-intrusive reduced order model (DDNIROM) is presented. The motivation of this work is to improve the capability of our recently developed NIROM [28, 34] for complex flow problems over widely varying range of scales (for example, from building, street to city scale). This can be done by partitioning the whole spatial computational domain into subdomains, thus capturing the details of local flow features characterized by these subdomains. Using POD, the local basis functions are generated based on the local solution snapshots over each subdomain. The RBF is then used for constructing a set of local hypersurfaces for each subdomain. These hypersurfaces include the fluid dynamics not only from the subdomain itself, but also from the neighboring subdomains.

The DDNIROM has been applied to two numerical test cases: flow past a cylinder and street canyon. Different number of basis functions were used for the subdomains. A comparison between the high fidelity full model, NIROM and DDNIROM has been conducted. The numerical results show that the DDNIROM exhibits comprehensive good agreement with the high fidelity full model and used fewer basis functions to attain same accuracy as the global NIROM.

This subdomain non-intrusive reduced order modelling is a generic and efficient approach for model reduction of general linear and non-linear time-dependent flow dynamical systems, even if where the source code is not available. Over existing global ROMs, the DDNIROM proposed here is able to (1) provide more details of local flows since local POD basis functions are generated based on local flow solutions over each subdomain and associated surrounding domains; (2) reduce the need for large multi-dimensional hypersurfaces representing the fluid dynamics using the global NIROM; and (3) reduce the size of the singular value decomposition and provide a greater scope for parallelization of the SVD. This is an essential step towards applying NIROMs to a real-life scenario with arbitrarily complex physics, *e.g.* traffic, chemistry, greening, particles and radiation.

Acknowledgments

The authors are grateful for the support of the EPSRC grant: Managing Air for Green Inner Cities (MAGIC)(EP/N010221/1) and the EPSRC MEMPHIS multi-phase flow programme grant (EP/K003976/1) and funding from the European Union Seventh Frame work Programme (FP7/20072013) under grant agreement No.603663 for the research project PEARL (Preparing for Extreme And Rare events in coastal regions).

References

[1] J Oliver, M Caicedo, AE Huespe, JA Hernández, and E Roubin. Reduced order modeling strategies for computational multiscale fracture. *Computer Methods in Applied Mechanics and Engineering*, 313:560–595, 2017.

[2] Bernd R Noack, Konstantin Afanasiev, Marek Morzynski, Gilead Tadmor, and Frank Thiele. A hierarchy of low-dimensional models for the transient and post-transient cylinder wake. *Journal of Fluid Mechanics*, 497:335–363, 2003.

[3] Bernd R Noack, Witold Stankiewicz, Marek Morzyński, and Peter J Schmid. Recursive dynamic mode decomposition of transient and post-transient wake flows. *Journal of Fluid Mechanics*, 809:843–872, 2016.

[4] Xuping Xie, David Wells, Zhu Wang, and Traian Iliescu. Approximate deconvolution reduced order modeling. *Computer Methods in Applied Mechanics and Engineering*, 313:512–534, 2017.

[5] Stefano Lorenzi, Antonio Cammi, Lelio Luzzi, and Gianluigi Rozza. Pod-galerkin method for finite volume approximation of navier–stokes and rans equations. *Computer Methods in Applied Mechanics and Engineering*, 311:151–179, 2016.

[6] Yuepeng Wang, Ionel M Navon, Xinyue Wang, and Yue Cheng. 2d burgers equation with large reynolds number using pod/deim and calibration. *International Journal for Numerical Methods in Fluids*, 82(12):909–931, 2016.

[7] B. R. Noack, M. Morzynski, and G. Tadmor. *Reduced-Order modelling for flow control*, volume 528. Springer, 2011.

[8] F Fang, T Zhang, D Pavlidis, C.C. Pain, AG Buchan, and I.M. Navon. Reduced order modelling of an unstructured mesh air pollution model and application in 2d/3d urban street canyons. *Atmospheric Environment*, 96:96–106, 2014.

[9] K.C. Hoang, Y. Fu, and J.H. Song. An hp-proper orthogonal decomposition-moving least squares approach for molecular dynamics simulation. *Computer Methods in Applied Mechanics and Engineering*, 298:548 – 575, 2016.

[10] Andrea Manzoni, Filippo Salmoiraghi, and Luca Heltai. Reduced basis isogeometric methods (rb-iga) for the real-time simulation of potential flows about parametrized naca airfoils. *Computer Methods in Applied Mechanics and Engineering*, 284:1147–1180, 2015.

[11] H Al Akhras, T Elguedj, A Gravouil, and M Rochette. Towards an automatic isogeometric analysis suitable trivariate models generationapplication to geometric parametric analysis. *Computer Methods in Applied Mechanics and Engineering*, 2016.

[12] Francesco Ballarin, Elena Faggiano, Sonia Ippolito, Andrea Manzoni, Alfio Quarteroni, Gianluigi Rozza, and Roberto Scrofani. Fast simulations of patient-specific haemodynamics of coronary artery bypass grafts based on a pod–galerkin method and a vascular shape parametrization. *Journal of Computational Physics*, 315:609–628, 2016.

[13] Michael Schlegel and Bernd R. Noack. On long-term boundedness of Galerkin models. *Journal of Fluid Mechanics*, 765:325–352, 2 2015.

[14] Jan Osth, Bernd R. Noack, SiniÅa Krajnovi, Diogo Barros, and Jacques Bore. On the need for a nonlinear subscale turbulence term in POD models as exemplified for a high-Reynolds-number flow over an Ahmed body. *Journal of Fluid Mechanics*, 747:518–544, 5 2014.

[15] Leopoldo P. Franca and Sergio L. Frey. Stabilized finite element methods: Ii. the incompressible Navier-Stokes equations. *Computer Methods in Applied Mechanics and Engineering*, 99(2-3):209–233, 1992.

[16] S. Chaturantabut and D.C. Sorensen. Nonlinear model reduction via discrete empirical interpolation. *SIAM J. Sci. Comput*, 32:2737–2764, 2010.

[17] Dunhui Xiao. *Non-intrusive reduced order models and their applications*. PhD thesis, Imperial College London, 2016.

[18] F.Fang, C.Pain, I.M. Navon, A.H. Elsheikh, J. Du, and D.Xiao. Non-linear Petrov-Galerkin methods for Reduced Order Hyperbolic Equations and Discontinuous Finite Element Methods. *Journal of Computational Physics*, 234:540–559, 2013.

[19] D. Xiao, F. Fang, J. Du, C.C. Pain, I.M. Navon, A. G. Buchan, A.H. ElSheikh, and G. Hu. Non-linear Petrov-Galerkin methods for reduced order modelling of the Navier-Stokes equations using a mixed finite element pair. *Computer Methods In Applied Mechanics and Engineering*, 255:147–157, 2013.

[20] C. Bou-Mosleh K. Carlberg and C. Farhat. Efficient non-linear model reduction via a least-squares petrov-galerkin projection and compressive tensor approximations. *International Journal for Numerical Methods in Engineering*, 86:155–181, 2011.

[21] M. Serpas Y. Chu and J. Hahn. State-preserving nonlinear model reduction procedure. *Chemical Engineering Science*, 66:3907–3913, 2011.

[22] Alireza Jafarpour Feriedoun Sabetghadam. α Regularization of the POD-Galerkin dynamical systems of the Kuramoto-Sivashinsky equation. *Applied Mathematics and Computation*, 218:6012–6026, 2012.

[23] Karen Willcox and Alexandre Megretski. Model reduction for large-scale linear applications. In *Proc. of 13th IFAC Symposium on System Identification, Rotterdam, Netherlands*, pages 1431–1436, 2003.

[24] M. Barrault, Y. Maday, N.C. Nguyen, and A.T. Patera. An empirical interpolation method: application to efficient reduced-basis discretization of partial differential equations. *C. R. Acad. Sci. Paris, Ser*, 339:667–672, 2004.

[25] D. Xiao, F. Fang, A. G. Buchan, C.C. Pain, I.M. Navon*, J. Du, , and G. Hu. Non-linear model reduction for the Navier-Stokes equations using Residual DEIM method. *Journal of Computational Physics*, 263:1–18, 2014.

[26] Kevin Carlberg, Charbel Farhat, Julien Cortial, and David Amsallem. The GNAT method for nonlinear model reduction: effective implementation and application to computational fluid dynamics and turbulent flows. *Journal of Computational Physics*, 242:623–647, 2013.

[27] Juan Du, Fangxin Fang, Christopher C Pain, I.M. Navon, Jiang Zhu, and David A Ham. POD reduced-order unstructured mesh modeling applied to 2d and 3d fluid flow. *Computers and Mathematics with Applications*, 65(3):362–379, 2013.

[28] D. Xiao, F. Fang, A.G. Buchan, C.C. Pain, I.M. Navon, and A. Muggeridge. Non-intrusive reduced order modelling of the Navier–Stokes equations. *Computer Methods in Applied Mechanics and Engineering*, 293:552–541, 2015.

[29] D. Xiao, F. Fang, C. Pain, and G. Hu. Non-intrusive reduced order modelling of the Navier-Stokes equations based on RBF interpolation. *International Journal for Numerical Methods in Fluids*, 79(11):580–595, 2015.

[30] S Walton, O Hassan, and K Morgan. Reduced order modelling for unsteady fluid flow using proper orthogonal decomposition and radial basis functions. *Applied Mathematical Modelling*, 37(20):8930–8945, 2013.

[31] C.Audouze, F.D.Vuyst, and P.B.Nair. Nonintrusive reduced-order modeling of parametrized time-dependent partial differential equations. *Numerical Methods for Partial Differential Equations*, 29(5):1587–1628, 2013.

[32] DA Bistrian and IM Navon. Randomized dynamic mode decomposition for non-intrusive reduced order modelling. *International Journal for Numerical Methods in Engineering*, 2016.

[33] D Xiao, P Yang, F Fang, J Xiang, CC Pain, and IM Navon. Non-intrusive reduced order modeling of fluid-structure interactions. *Computer Methods in Applied Mechanics and Engineering*, 303:35–54, 2016.

[34] D Xiao, P Yang, F Fang, J Xiang, CC Pain, IM Navon, and M Chen. A non-intrusive reduced-order model for compressible fluid and fractured solid coupling and its application to blasting. *Journal of Computational Physics*, 330:221–244, 2017.

[35] D Xiao, Z Lin, F Fang, C C Pain, Ionel M Navon, P Salinas, and A Muggeridge. Non-intrusive reduced-order modeling for multiphase porous media flows using smolyak sparse grids. *International Journal for Numerical Methods in Fluids*, 83(2):205–219, 2017.

[36] D Xiao, F Fang, C Pain, IM Navon, and A Muggeridge. Non-intrusive reduced order modelling of waterflooding in geologically heterogeneous reservoirs. In *ECMOR XV-15th European Conference on the Mathematics of Oil Recovery*, 2016.

[37] D. Xiao, F. Fang, C.C. Pain, and I.M. Navon. A parameterized non-intrusive reduced order model and error analysis for general time-dependent nonlinear partial differential equations and its applications. *Computer Methods in Applied Mechanics and Engineering*, 317:868–889, 2017.

[38] David J Lucia, Paul I King, and Philip S Beran. Reduced order modeling of a two-dimensional flow with moving shocks. *Computers & Fluids*, 32(7):917–938, 2003.

[39] Janusz S Przemieniecki. Matrix structural analysis of substructures. *AIAA Journal*, 1(1):138–147, 1963.

[40] IM Navon and Y Cai. Domain decomposition and parallel processing of a finite element model of the shallow water equations. *Computer methods in applied mechanics and engineering*, 106(1-2):179–212, 1993.

[41] Y Cai and IM Navon. Parallel block preconditioning techniques for the numerical simulation of the shallow water flow using finite element methods. *Journal of Computational Physics*, 122(1):39–50, 1995.

[42] Luc Berger-Vergiat and Haim Waisman. An overlapping domain decomposition preconditioning method for monolithic solution of shear bands. *Computer Methods in Applied Mechanics and Engineering*, 318:33–60, 2017.

[43] Søren Taverniers and Daniel M Tartakovsky. A tightly-coupled domain-decomposition approach for highly nonlinear stochastic multiphysics systems. *Journal of Computational Physics*, 330:884–901, 2017.

[44] Xin Bian, Zhen Li, and George Em Karniadakis. Multi-resolution flow simulations by smoothed particle hydrodynamics via domain decomposition. *Journal of Computational Physics*, 297:132–155, 2015.

[45] Joan Baiges, Ramon Codina, and Sergio Idelsohn. A domain decomposition strategy for reduced order models. application to the incompressible navier–stokes equations. *Computer Methods in Applied Mechanics and Engineering*, 267:23–42, 2013.

[46] David Amsallem, Matthew J Zahr, and Charbel Farhat. Nonlinear model order reduction based on local reduced-order bases. *International Journal for Numerical Methods in Engineering*, 92(10):891–916, 2012.

[47] Saifon Chaturantabut. Temporal localized nonlinear model reduction with a priori error estimate. *Applied Numerical Mathematics*, 2017.

[48] Pierre Kerfriden, Olivier Goury, Timon Rabczuk, and Stephane Pierre-Alain Bordas. A partitioned model order reduction approach to rationalise computational expenses in nonlinear fracture mechanics. *Computer methods in applied mechanics and engineering*, 256:169–188, 2013.

[49] George Shu Heng Pau, Chaopeng Shen, William J Riley, and Yaning Liu. Accurate and efficient prediction of fine-resolution hydrologic and carbon dynamic simulations from coarse-resolution models. *Water Resources Research*, 2016.

[50] GSH Pau, G Bisht, and WJ Riley. A reduced-order modeling approach to represent subgrid-scale hydrological dynamics for land-surface simulations: application in a polygonal tundra landscape. *Geoscientific Model Development*, 7(5):2091–2105, 2014.